Chinese Chemical Letters 35 (2024) 109219

Contents lists available at ScienceDirect

Chinese Chemical Letters

journal homepage: www.elsevier.com/locate/cclet

Regulating the electronic structure of Ir single atoms by ZrO_2 nanoparticles for enhanced catalytic oxidation of formaldehyde at room temperature

Shiqi Peng[a,b], Yongfang Rao[c], Tan Li[d,e], Yufei Zhang[f,*], Jun-ji Cao[b,g], Shuncheng Lee[h], Yu Huang[a,i,*]

[a] Key Laboratory of Aerosol Chemistry & Physics, State Key Laboratory of Loess and Quaternary Geology (SKLLQG), Institute of Earth Environment, Chinese Academy of Sciences (CAS), Xi'an 710061, China
[b] School of Human Settlements and Civil Engineering, Xi'an Jiaotong University, Xi'an 710049, China
[c] Department of Environmental Science and Engineering, Xi'an Jiaotong University, Xi'an 710049, China
[d] Faculty of Chemical Engineering, Kunming University of Science and Technology, Kunming 650500, China
[e] School of Environment and Energy, South China University of Technology, Guangzhou 51006, China
[f] School of Environmental and Municipal Engineering, Xi'an University of Architecture and Technology, Xi'an 710055, China
[g] Institute of Atmospheric Physics, Chinese Academy of Sciences, Beijing 100190, China
[h] Department of Civil and Environmental Engineering, The Hong Kong Polytechnic University, Hong Kong, China
[i] CAS Center for Excellence in Quaternary Science and Global Change, Xi'an 710061, China

ARTICLE INFO

Article history:
Received 28 June 2023
Revised 19 September 2023
Accepted 16 October 2023
Available online 20 October 2023

Keywords:
ZrO_2 nanoparticles
Ir single atoms
Electronic structure
Formaldehyde
Catalytic oxidation

ABSTRACT

Developing low-loading single-atom catalysts with superior catalytic activity and selectivity in formaldehyde (HCHO) oxidation at room temperature remains challenging. Herein, ZrO_2 nanoparticles coupled low-loading Ir single atoms in N-doped carbon (Ir_1-N-C/ZrO_2) was prepared. The optimal Ir_1-N-C/ZrO_2 with 0.25 wt% Ir loading delivers the high HCHO removal and conversion efficiency (>95%) at 20 °C, which is higher than that over Ir_1-N-C with the same Ir loading. The specific rate can reach 1285.6 mmol g_{Ir}^{-1} h^{-1}, surpassing the Ir based catalysts reported to date. Density functional theory calculation results and electron spin resonance spectra indicate that the introduction of ZrO_2 nanoparticles modulate the electronic structure of the Ir single atoms, promoting O_2 activation to $^{\bullet}O_2^-$. Moreover, the Ir-C-Zr channel is favorable for the dissociation of $^{\bullet}O_2^-$ to active oxygen atom ($^*O$), and further accelerates the transformation of HCHO and intermediates (dioxymethylene and formates) to CO_2 and H_2O. This work provides a facile strategy to design low-loading single-atom catalysts with high catalytic activity toward HCHO oxidation.

Formaldehyde (HCHO) as a primary indoor gas pollutant can increase the risk of asthma, dyspnea, or even teratogenesis and carcinogenesis [1]. The concentration of indoor HCHO is usually in the sub-ppm or ppb range. But in some newly refurbished rooms, the concentration of HCHO may reach several hundred ppm [2]. Numerous available methods have been adopted for HCHO elimination [3]. Catalytic oxidation at room temperature is an effective strategy since no external energy (light, heat, *etc.*) is demanded. HCHO molecules can be oxidized by reactive oxygen species (ROS) and mineralized into CO_2 and H_2O over catalysts [4–7]. Principally, noble-metals have been regarded as the most active catalyst as they are capable of O_2 activation at room temperature [8,9]. However, due to the rarity of noble-metals, modulating the microstructures of noble-metals plays a crucial role in determining the catalytic efficiency.

Geometrically, single-atom catalysts (SACs) have realized the maximum atomic utilization efficiency [10]. The unique low-coordination environments facilitate the adsorption of reactants. Our previous work [11] has demonstrated that N-doped carbon octahedron supported iridium single atoms (Ir_1-N-C) with 1.6 wt% Ir loading can achieve high HCHO removal and conversion efficiency (~97%) in 760 min at 20 °C. When the Ir loading decreases to 0.5 wt%, the HCHO conversion efficiency only reaches 42.7%. The weak O_2 activation capacity over low-loading Ir single atoms leads to an incomplete conversion of HCHO. O_2 could only be activated into $^{\bullet}O_2^-$, which slows down the reaction rate. How to im-

* Corresponding authors.
E-mail addresses: zhangyufei@xauat.edu.cn (Y. Zhang), huangyu@ieecas.cn (Y. Huang).

https://doi.org/10.1016/j.cclet.2023.109219
1001-8417/

prove O_2 activation capacity of low-loading Ir_1-N-C has become a challenge. Previous studies have explored two routes for improving the catalytic activity of SACs: increasing the density of active sites [12–14] and improving the intrinsic activity of the active sites [15]. Therefore, seeking the effective ways to improve the intrinsic activity of Ir single atoms may be a feasible strategy. Combing inorganic particles with M_1-N-C (M: transition metal) could optimize the electronic structure and the high catalytic activity is expected. In the preparation of M_1-N-C by pyrolysis of metal–organic frameworks (MOF), the inorganic particles (such as transition metal carbide, nitride and oxide, metal particles, *etc.*) were generated simultaneously. These inorganic particles may play a positive role in catalytic activity. Cheng *et al.* [16]. found that the iron nitride combined with the iron and nitrogen co-doped carbon layer (Fe_xN@Fe-N-C) selectively enhanced the activity of Fe-N-C toward CO_2 reduction reaction (CO_2RR). The introduction of Fe_xN could regulate the balance between the adsorption and desorption of CO. The same group also reported the promoted O_2 reduction reaction over Co@Co-N-C compared with that over Co-N-C due to the downshift of the d-band center of Co nanoparticles [17,18]. Nanostructured ZrO_2 was reported to cooperate with single-atom Ni-N-C to drive electrochemical CO_2RR, where the Ni-N_4 species was the real active sites and the nano-ZrO_2 accelerated the protonation of intermediate products. In addition, Zhang *et al.* [19]. constructed the hybrid catalyst containing ZrO_2 nanoclusters and Fe-N-C. ZrO_2 nanoclusters can improve O_2 adsorption capacity and ORR activity, which was attributed to the strong interaction between ZrO_2 and the isolated Fe single atom.

Motivated by the strategy, a catalyst containing ZrO_2 nanoparticles coupled Ir single atoms in N doped carbon (Ir_1-N-C/ZrO_2) was prepared by *in situ* pyrolysis of UiO-66-NH_2 adsorbed Ir ions. The reference Ir_1-N-C was obtained by etching ZrO_2 in HF solution. The presence of ZrO_2 nanoparticles was expected to promote the catalytic activity of Ir_1-N-C. The electronic structure of Ir_1-N-C/ZrO_2 was characterized by X-ray photoelectron spectroscopy (XPS), electron spin resonance (ESR) and density functional theory (DFT) calculations. The effect of ZrO_2 on O_2 adsorption and activation was investigated by temperature-programmed technique and DFT calculations. Furthermore, *in situ* diffuse reflectance infrared Fourier transform spectroscopy demonstrated the HCHO oxidation mechanism.

Ir_1-N-C/ZrO_2 was derived from UiO-66–NH_2 adsorbed Ir ions (Fig. 1a). N atoms of $-NH_2$ can readily trap the adsorbed Ir ions and form isolated Ir-N_4 coordination during the pyrolysis process. The $[Zr_6(\mu_3\text{-}O)_4(\mu_3\text{-}OH)_4]^{12+}$ nodes were transformed to ultrasmall ZrO_2 nanoparticles and H_2BDC-NH_2 linker were decomposed into N-doped carbon skeleton [11].

According to the XRD patterns (Fig. 1b), Ir_1-N-C/ZrO_2 displays the typical tetragonal zirconia structure (t-ZrO_2, PDF No. 49-1642) [20]. The broad diffraction peak at 23° is corresponded to the (002) plane of amorphous graphitic carbon [21]. The t-ZrO_2 crystallites are dispersed in graphitic carbon. The average crystallite size of t-ZrO_2 was determined to be 5.7 nm using Scherrer's equation and the (111) peak. For Ir_1-N-C prepared by HF etching, the XRD characteristic peaks of t-ZrO_2 disappear and Ir_1-N-C displays a typical XRD patterns of graphitic carbon.

Ir_1-N-C/ZrO_2 inherits the recognizable octahedral configuration of Ir/UiO-66–NH_2 (Fig. S1 in Supporting information). This is further verified by aberration-corrected high angle annular dark-field scanning transmission electron microscope (HAADF-STEM, Fig. 1c). The average diameter of Ir_1-N-C/ZrO_2 is approximately 200–300 nm. The magnified HAADF-STEM image (Fig. 1d) revealed that the particle sizes of ZrO_2 nanoparticles are about 4.0 nm. This is because the carbon skeleton could build a barrier to hinder the aggregation of ZrO_2 nanoparticles during pyrolysis. And the lattice fringe spacing of 0.295 nm is assigned to the (011) plane of

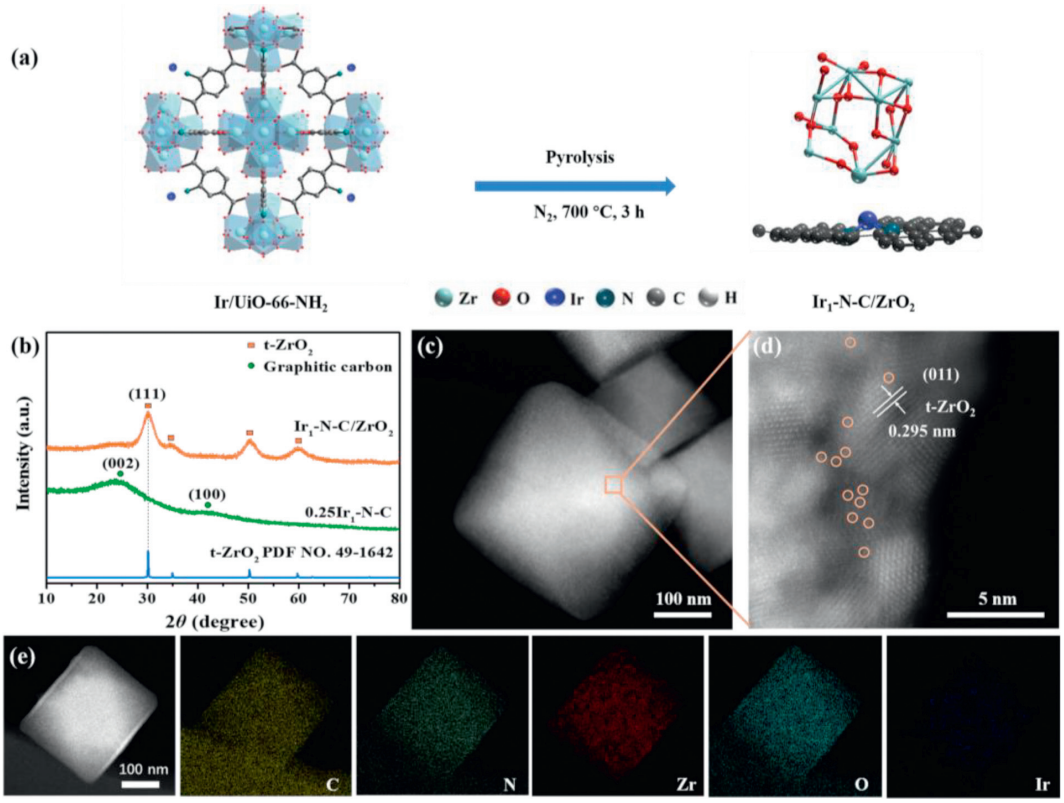

Fig. 1. (a) Schematic illustration of the synthesis procedure of Ir_1-N-C/ZrO_2. (b) XRD patterns of Ir_1-N-C/ZrO_2 and Ir_1-N-C. (c) HAADF-STEM image of Ir_1-N-C/ZrO_2. (d) High-resolution HAADF-STEM image of Ir single atoms of Ir_1-N-C/ZrO_2. (e) STEM-EDX element mapping for C, N, Zr, O and Ir of Ir_1-N-C/ZrO_2.

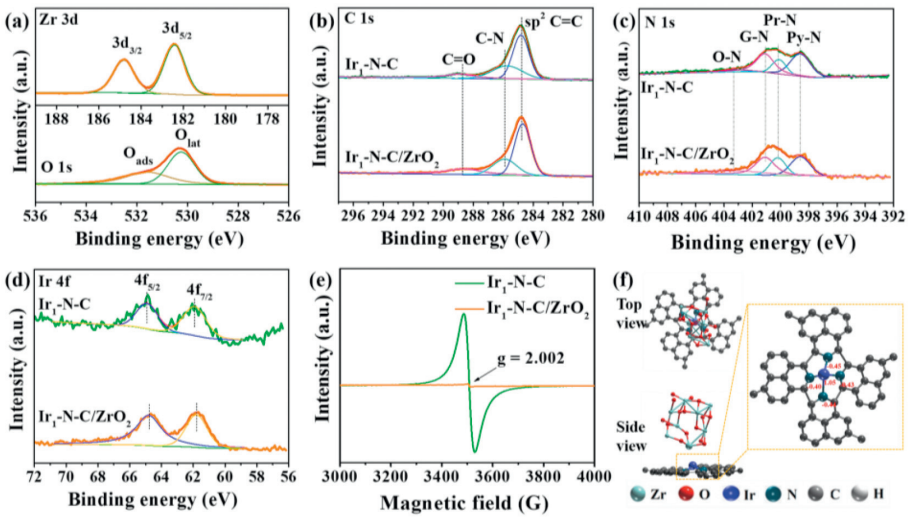

Fig. 2. (a) High-resolution Zr 3d XPS spectra and O 1s XPS spectra of Ir_1-N-C/ZrO_2. High-resolution XPS spectra of Ir_1-N-C/ZrO_2 and Ir_1-N-C: (b) C 1s, (c) N 1s, and (d) Ir 4f. (e) ESR spectra of Ir_1-N-C/ZrO_2 and Ir_1-N-C. (f) Mulliken charge of Ir_1-N-C/ZrO_2.

a typical t-ZrO_2 [22]. The bright spots within the yellow ring areas are assigned to the isolated Ir atoms, indicating atomic dispersion of Ir on the carbon support. All of C, N, Zr, O and Ir elements are uniformly distributed within the entire octahedral matrix, as demonstrated by the STEM energy-dispersive X-ray spectroscopy (EDX) element mapping (Fig. 1e). Meanwhile, After HF etching, the HAADF-STEM image of Ir_1-N-C maintains a similar octahedral morphology. The atomically isolated Ir atoms can be clearly observed on the N-C support (Fig. S2 in Supporting information), indicating that the ZrO_2 nanoparticles were completely removed.

In order to investigate the changes of electronic properties of Ir single atoms, the surface chemical states of Ir_1-N-C/ZrO_2 were analyzed by XPS and ESR technique. Ir_1-N-C/ZrO_2 exhibits a spin-orbit doublet of the Zr 3d core level into $3d_{5/2}$ and $3d_{3/2}$ levels with an energy gap of 2.4 eV. The $3d_{5/2}$ and $3d_{3/2}$ binding energies locate at 182.3 eV and 184.7 eV (Fig. 2a). Compared with the high-resolution spectra of Zr 3d (182.2 for $3d_{5/2}$ and 184.6 eV for $3d_{3/2}$) of N-C/ZrO_2 (Fig. S3 in Supporting information), the Zr 3d XPS spectrum of Ir_1-N-C/ZrO_2 shifts to higher binding energy. Combined with the high-resolution XPS spectra of O 1s, the characteristic peaks located at 529.8 eV and 531.2 eV are corresponded to lattice oxygen (O_{lat}) and surface adsorption oxygen species (O_{ads}), respectively [23], which proves that ZrO_2 in Ir_1-N-C/ZrO_2 conforms to the stoichiometric ratios [24]. Furthermore, the O 1s high-resolution XPS spectra of Ir_1-N-C/ZrO_2 and N-C/ZrO_2 were analyzed. The surface molar ratio of O_{ads}/O_{lat} of Ir_1-N-C/ZrO_2 is 1.3, higher than that of 1.1 of N-C/ZrO_2 indicating that the introduction of Ir single atom favors the formation of surface adsorbed oxygen. The fine C 1s spectrum shows three carbon species: sp^2-hybridized structure (284.6 eV), C-N groups (286.0 eV), and carboxyl groups (288.7 eV) [23] (Fig. 2b). C atoms in the carbon carrier mainly exist in the form of sp^2 hybridization, which is consistent with the graphitized carbon carrier characterized in the XRD pattern. The high-resolution broad N 1s spectrum is fitted into four components, which are associated with pyridinic N (Py-N, 398.6 eV), pyrrolic N (Pr-N, 400.1 eV), graphitic N (G-N, 401.1 eV), and oxidized N (O-N, 403.1 eV) [17] (Fig. 2c). The ratio of Py-N/total N of Ir_1-N-C/ZrO_2 and Ir_1-N-C were 0.41 and 0.44, respectively. Furthermore, the high-resolution Ir 4f spectra of Ir_1-N-C can be deconvoluted into Ir $4f_{7/2}$ and Ir $4f_{5/2}$ spin-orbit doublets centered at 61.9 eV and 64.9 eV, which could be attributed to the predominant oxidation state of $Ir^{\delta+}$ [25] (Fig. 2d). The Ir $4f_{7/2}$ and Ir $4f_{5/2}$ spin-orbit doublets of Ir_1-N-C/ZrO_2 shift to lower binding energies (61.8 eV and 64.8 eV), indicating that the electron density close to Ir single atoms increases. Combined with the above results, it can be speculated that Ir species in Ir_1-N-C/ZrO_2 exist in the form of single atoms, without Ir nanoparticles or clusters. Ir single atoms mainly exist in the coordination of Ir-N_4. The surface chemical states of Ir single atoms changed, suggesting that the Ir-C-Zr channel formed.

ESR spectroscopy was further used to study the unpaired electrons of Ir_1-N-C/ZrO_2. As shown in Fig. 2e, for Ir_1-N-C, a single Lorentzian line with a g value of 2.002 was observed (Fig. 2e), which can be assigned to the unpaired electron of N-doped carbon [26]. When introduced ZrO_2 nanoparticles, the intensity of the narrow peak of $g = 2.002$ decreased significantly. The decreasing ESR signal reveals that less lone electrons resided in Ir_1-N-C/ZrO_2 and electrons become more localized. Based on DFT calculation, the Mulliken charge of Ir atom for Ir_1-N-C/ZrO_2 is positive (1.05) (Fig. 2f), lower than that of Ir_1-N-C reported in our previous work (1.12) [11]. The results are consistent with these of the high-resolution Ir 4f spectra. These above results mean that after interact with ZrO_2, the Ir is more electron deficient, so there forms a localized electronic state around Ir atom, which provides an electron donor active site for the subsequent catalytic reaction.

The promotional effect of ZrO_2 nanoparticles on HCHO oxidation was investigated. The HCHO oxidation was evaluated under ambient conditions (Atmospheric pressure, $T = 20$ °C) in terms of HCHO removal (η) and HCHO conversion (X). As shown in Figs. 3a and b, Ir_1-N-C/ZrO_2 displays the highest η and X values. After 120 min, the η values of all samples are higher than 80%, which can be ranked as Ir_1-N-C/ZrO_2 > Ir_1-N-C + ZrO_2 (Fig. S4 in Supporting information) > Ir_1-N-C > N-C/ZrO_2. The X values of these samples were quite different. Ir_1-N-C/ZrO_2 exhibits a remarkable HCHO oxidation performance with X of 95.6%, compared to Ir_1-N-C (20.6%), indicating that ZrO_2 nanoparticles play a positive role in promoting HCHO oxidation performance. In contrast, the pristine N-C/ZrO_2 without Ir species exhibits inferior catalytic activity (η = 94.1%, $X = 15.8\%$). This could be ascribed to the porous structure and N species favorable for the efficient HCHO adsorption. ZrO_2 mainly contributes to HCHO conversion. But the X values gradually decreased within 2 h (Figs. S5, S6 and S7 in Supporting information), indicating that Ir single atoms were the main reactive active sites. In addition, the physical mixture of Ir_1-N-C + ZrO_2 shows lower catalytic activity ($\eta = 86.3\%$, $X = 55.7\%$), suggesting the interaction between isolated Ir atoms and ZrO_2 nanoparticles instead of mechanical mixing in Ir_1-N-C/ZrO_2.

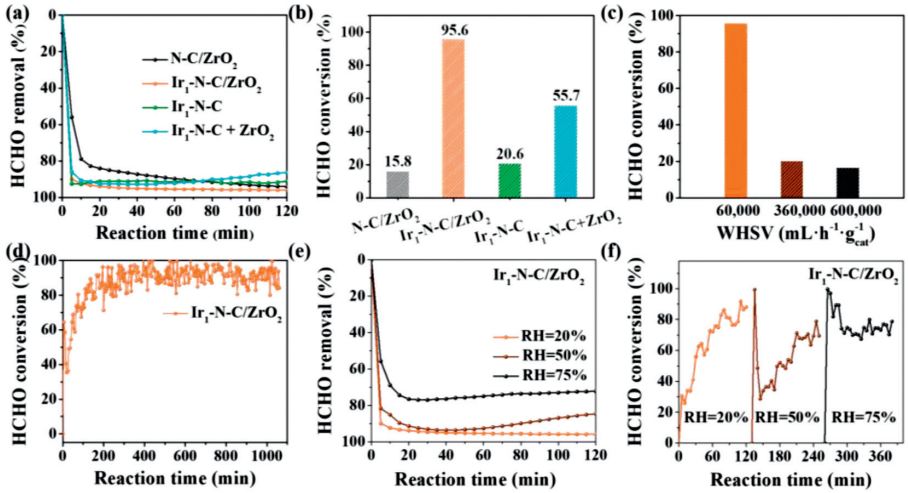

Fig. 3. (a) HCHO removal as a function of time over Ir_1-N-C/ZrO_2, Ir_1-N-C + ZrO_2, Ir_1-N-C and N-C/ZrO_2. (b) HCHO conversion of Ir_1-N-C/ZrO_2, Ir_1-N-C + ZrO_2, Ir_1-N-C and N-C/ZrO_2 after 2 h test. (c) HCHO conversion of Ir_1-N-C/ZrO_2 under different WHSV. (d) Stability test over Ir_1-N-C/ZrO_2. Reaction conditions: 20 °C, 100 ppm HCHO, 20 vol% O_2, and N_2 balance, relative humidity (RH): 20%, WHSV: 60,000 mL h^{-1} g_{cat}^{-1}. (e) HCHO removal and (f) HCHO conversion over Ir_1-N-C/ZrO_2 under the RH of 20%, 50% and 75%.

Table 1
Catalytic activities of HCHO oxidation over the Ir-based catalysts in continuous-flow fixed-bed reactor reported in literatures.

Catalyst	Ir loading (wt%)	T (°C)	Reaction condition	R (mmol g_{Ir}^{-1} h^{-1})	Note
Ir_1-N-C/ZrO_2	0.25	20	100 ppm HCHO, 20% O_2, N_2 balance, RH = 25%	1285.6	This work
Ir_1-N-C	0.26	20	100 ppm HCHO, 20% O_2, N_2 balance, RH = 25%	21.4	This work
Ir/Al_2O_3	1.50	20	180 ppm HCHO, 20% O_2, He balance, RH = 50%	79.2	[24]
Ir/Al_2O_3	1.80	20	180 ppm HCHO, 20% O_2, He balance, RH = 50%	43.5	[24]
Na-Ir/TiO_2	0.95	25	120 ppm HCHO, 20% O_2, He balance, RH = 50%	159.0	[25]

The intrinsic activities of Ir_1-N-C/ZrO_2 and Ir_1-N-C catalysts were also compared by calculating the specific rates (R) values. R value was calculated when X value reaches 20% (Fig. 3c). R value of Ir_1-N-C/ZrO_2 was calculated as 1285.6 mmol g_{Ir}^{-1} h^{-1} when the weight hourly space velocity (WHSV) was set as 360,000 mL h^{-1} g_{cat}^{-1} after 120 min, surpassing that of Ir_1-N-C (21.4 mmol g_{Ir}^{-1} h^{-1}) when the WHSV was set as 60,000 mL h^{-1} g_{cat}^{-1}. The R value of Ir_1-N-C/ZrO_2 was also higher than the values of 43.5 mmol g_{Ir}^{-1} h^{-1} (1.8 wt% Ir/Al_2O_3), 79.2 mmol g_{Ir}^{-1} h^{-1} (1.5 wt% Ir/Al_2O_3) [27] and 159.0 mmol g_{Ir}^{-1} h^{-1} (0.95 wt% Na-Ir/TiO_2) [28] reported in previous studies (Table 1). Based on these above results, the Ir_1-N-C/ZrO_2 outperformed most Ir-based catalysts reported hitherto. The long-term stability of the catalyst is also an important factor for the evaluation of the catalyst. Fig. 3d shows the catalytic activity of Ir_1-N-C/ZrO_2 maintained as long as 1000 min. The HCHO conversion is about 95%, indicating that Ir_1-N-C/ZrO_2 has good catalytic long-term stability. In addition, the effect of humidity on the catalytic performance of Ir_1-N-C/ZrO_2 was measured under the relative humidity of 20%, 50% and 75% (Figs. 3e and f). The HCHO conversion still kept above 80% when the RH increased to 75%, indicating the catalyst has excellent moisture resistance. When the RH increased from 50% to 75%, more water molecules competed with HCHO molecules over the surface of Ir_1-N-C/ZrO_2. The decreasing adsorbed HCHO molecules may result in a low η value. However, when the RH increased from 50% to 75%, the increasing water molecules may react with the active oxygen atoms and form hydroxyl groups. The highly reactive hydroxyl groups may promote the conversion of adsorbed HCHO molecules into CO_2.

To understand the mechanisms underlying the promoting effect of ZrO_2 nanoparticles on HCHO oxidation, the relationship between the structure and catalytic activity of Ir_1-N-C/ZrO_2 and Ir_1-N-C was investigated. N_2 sorption–desorption experiment was conducted to analyze the texture structure of Ir_1-N-C/ZrO_2 and Ir_1-N-C (Fig. S8 in Supporting information). Both Ir_1-N-C/ZrO_2 and Ir_1-N-C samples show typical type IV adsorption and desorption isotherms. The isotherm of Ir_1-N-C/ZrO_2 has a H2-type hysteresis ring while the isotherm of Ir_1-N-C has a H3-type hysteresis loop, which leads to the different pore structures of the two samples. The Ir_1-N-C/ZrO_2 sample mainly possesses a large number of mesoporous pores with an average pore size of 12.7 nm. The pore size ensures that the HCHO and O_2 molecules could get to the active sites in the catalyst. Table S2 in Supporting information lists the specific surface area (S_{BET}), pore volume (V_p) and pore size (d_p) parameters of Ir_1-N-C/ZrO_2 and Ir_1-N-C. HCHO conversion efficiency over Ir_1-N-C/ZrO_2 and Ir_1-N-C was normalized by being divided by S_{BET}, and the results were 0.0685% and 0.0357% g/m^2, respectively. It can be seen that S_{BET} is not the only factor affecting the catalytic performance.

The oxygen species of Ir_1-N-C/ZrO_2 was studied by O_2-TPD, as shown in Fig. 4a. The O_2-TPD spectra can be divided into three regions: the desorption of surface adsorbed oxygen (<200 °C), the desorption of the surface lattice oxygen (200–400 °C) and the desorption of intrinsic lattice oxygen in bulk phase (>400 °C), respectively [29]. A small peak at 109 °C is observed for Ir_1-N-C/ZrO_2 from the 5-fold magnified figure, whereas no obvious peaks were observed for Ir_1-N-C and N-C/ZrO_2 at lower temperature below 200 °C. This indicates that more easily migrated surface adsorbed oxygen species were activated over Ir_1-N-C/ZrO_2. In the range of 200–400 °C, Ir_1-N-C/ZrO_2 and N-C/ZrO_2 show two obvious desorption peaks, respectively. The typical desorption peak of N-C/ZrO_2 was located at 341 °C, while 285 °C for Ir_1-N-C/ZrO_2. Compared to that of N-C/ZrO_2, the desorption peak of surface lattice oxygen of Ir_1-N-C/ZrO_2 appear at a lower temperature and the peak intensity

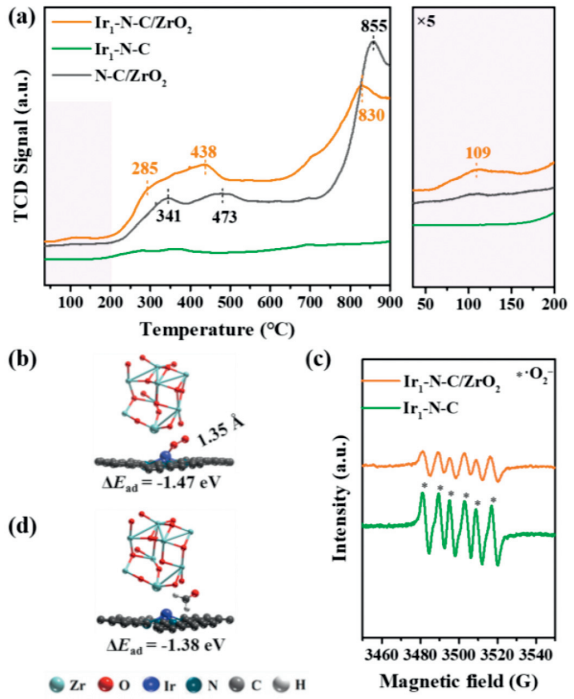

Fig. 4. (a) O_2-TPD profiles of Ir_1-N-C/ZrO_2, Ir_1-N-C and N-C/ZrO_2. (b) Side view of the most stable adsorption configurations of O_2 on Ir_1-N-C/ZrO_2. (c) DMPO spin-trapping ESR spectra of $\cdot O_2^-$ in methanol solution. (d) Side view of the most stable adsorption configurations of HCHO on Ir_1-N-C/ZrO_2.

become stronger, indicating that the interaction between Ir single atom and ZrO_2 promotes the activation of surface lattice oxygen over Ir_1-N-C/ZrO_2.

The adsorption behavior of O_2 molecule on the surface of Ir_1-N-C/ZrO_2 was further investigated by DFT calculation. O_2 molecule prefers to be adsorbed on Ir sites by the end-on adsorption pattern with the formation of Ir−O bonds and the adsorption energy of −1.47 eV (Fig. 4b), higher than that over Ir_1-N-C (−0.43 eV) [11]. The O-O bond is elongated to 1.35 Å. In comparation with Ir_1-N-C reported in our previous work, the high adsorption energy and elongated O-O bond manifested the promotional effect of ZrO_2 nanoparticles on O_2 adsorption. Furthermore, ESR technique was used to trace the reactive oxygen species (ROS) after O_2 adsorption (Fig. 4c). The DMPO/$^{\bullet}O_2^-$ adduct with characteristic six split lines (a_H = 7.7G, a_N = 13.6 G) [30] was observed for Ir_1-N-C. The signal attenuated significantly when ZrO_2 was introduced to Ir_1-N-C, indicating that the generation of $^{\bullet}O_2^-$ was significantly reduced or most $^{\bullet}O_2^-$ species was transformed into other oxygen species. Combined with XPS and O_2-TPD results, it is reasonable to speculate that the surface reactive oxygen species were generated after O_2 activation. In addition, the introduction of ZrO_2 increased the adsorption energy of HCHO molecule from 0.25 eV to −1.38 eV (Fig. 4d) [11].

The O_2 dissociation behavior and the activation energy of the major reaction paths of HCHO oxidation at the interface of Ir_1-N-C/ZrO_2 were calculated using DFT calculations [31] (Fig. 5a). The results show that O_2 obtains electrons and formed $^{\bullet}O_2^-$. Then $^{\bullet}O_2^-$ dissociates into $^*O$ by the Ir-C-Zr channel rapidly. The activation energy of the adsorbed O_2 dissociation at the interface of Ir_1-N-C/ZrO_2 is −1.0 eV or −23.06 kcal/mol (1 eV = 23.06 kcal/mol); then two active oxygen atoms ($^*O$) are generated, which can oxidize HCHO to form formic acid. Specifically, an $^*O_1$ produced by the dissociation of adsorbed O_2 begins to migrate to the interface between the Zr site of ZrO_2 (011) and Ir_1-N-C. Another $^*O_2$ is closer to the Zr site of ZrO_2 (011). The $^*O_1$ reacts with HCHO to form formic acid (HCOOH), the activation energy of

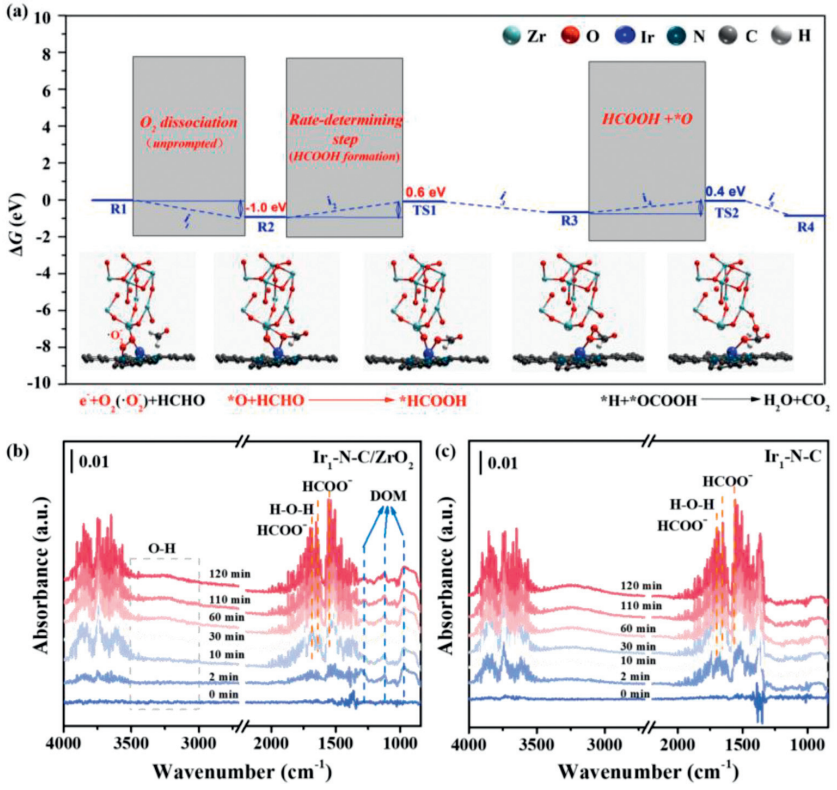

Fig. 5. (a) The activation energy of the major reaction path of HCHO oxidation transformed into CO_2 and H_2O at the Ir_1-N-C/ZrO_2 interface. *In situ* DRIFTS profiles of the samples (b) Ir_1-N-C/ZrO_2 supported on silica wool, and (c) Ir_1-N-C supported on silica wool.

which is 0.6 eV (13.84 kcal/mol). Furthermore, the $^*O_2$ reacts with HCOOH to form CO_2 and H_2O, the activation energy of which is 0.4 eV (9.22 kcal/mol). Thus, the activation energy of the rate-determination step of the major reaction path is 13.84 kcal/mol, which is less than our previous report results [32], and the rate-determining step is that the reactive $^*O_1$ near the Zr site of ZrO_2 (011) is transferred to the C atom in C-H bond of HCHO ($HCHO + {}^*O_1 \rightarrow HC^*O_1OH$). The formed reactive oxygen species could oxidize HCHO into DOM, formate species and CO_2 and H_2O rapidly.

In situ DRIFTS was further performed to monitor the intermediates generated in the catalytic process, revealing the reaction paths over Ir_1-N-C/ZrO_2 and Ir_1-N-C surfaces. All catalyst powders were dispersed onto an inert silica wool for testing. For Ir_1-N-C/ZrO_2 supported on silica wool, after the mixture of HCHO and air flow was introduced for 2 min, three obvious characteristic peaks appeared at 968, 1120 and 1290 cm^{-1}, which were attributed to ν(CO), $\rho(CH_2)$ and $\tau(CH_2)$ of dioxymethylene (DOM) species [33,34], respectively. As reaction time was prolonged, the characteristic peak intensity of DOM decreased; especially the intensity of characteristic peak at 1290 cm^{-1} decreased significantly. At the same time, the intensity of characteristic peak at 1560 cm^{-1} attributed to ν_{as}(OCO) of increased gradually, indicating that DOM was further oxidized to formate species. The bands in the range of 3250–4000 cm^{-1} originated from the gradual accumulation of water molecules and hydroxyl groups [34]. The DOM and formate species were the main intermediates generated in the reaction (Fig. 5b). In contrast, in terms of Ir_1-N-C supported on silica wool, the intensities of these characteristic peaks are extremely low under the same experimental conditions and the peaks at 1120 cm^{-1} and 1290 cm^{-1} vanished (Fig. 5c). The results indicate that only a small fraction of HCHO molecules were oxidized into DOM and the reactive oxygen species including $^{\bullet}O_2^-$ and surface oxygen species generated on the surface of Ir_1-N-C/ZrO_2 could oxidize HCHO into DOM and formate species rapidly.

Based on the DFT calculations and *in situ* DRIFTS results, the HCHO degradation pathways were proposed over Ir_1-N-C/ZrO_2. ZrO_2 nanoparticles and Ir single atoms synergistically enhanced HCHO oxidation at room temperature. O_2 was activated to $^{\bullet}O_2^-$ and surface oxygen species, which served as the key reactive oxygen species to oxidize HCHO to DOM, formate species and CO_2 and H_2O rapidly. However, on the surface of Ir_1-N-C, O_2 was mainly adsorbed and activated to generate $^{\bullet}O_2^-$.

To summarize, an effective strategy was proposed to improve the catalytic activity of low-loading Ir single atoms at room temperature. By engineering ZrO_2 nanoparticles with Ir single atoms in N-doped carbon (Ir_1-N-C/ZrO_2), the enhancing effect of ZrO_2 nanoparticles on HCHO oxidation was demonstrated by experimental results and DFT calculations. The specific reaction rate of 0.25 wt% Ir_1-N-C/ZrO_2 could reach as high as 1285.6 mmol g_{Ir}^{-1} h^{-1}, surpassing the Ir-based catalysts reported in previous studies. 0.26 wt% Ir_1-N-C only achieved a low specific reaction rate of 21.4 mmol g_{Ir}^{-1} h^{-1}. ZrO_2 nanoparticles can regulate the electronic property of Ir single atom through charge redistribution, synergistically promoting the activation of surface adsorption oxygen and surface lattice oxygen to generate reactive oxygen species. The Ir-C-Zr channel also accelerated the dissociation of $^{\bullet}O_2^-$ to active oxygen atom ($^*O$). The formed reactive oxygen species could oxidize HCHO to DOM, formate species and CO_2 and H_2O rapidly. In brief, our work offers a new way to obtain the low-loading single-atom catalyst with superior catalytic activity towards HCHO oxidation by rational design.

Declaration of competing interest

The authors declare that they have no known competing financial interests or personal relationships that could have appeared to influence the work reported in this paper.

Acknowledgments

This work was supported by the Strategic Priority Research Program of the Chinese Academy of Sciences, China (Nos. XDA23010300 and XDA23010000), National Science Foundation of China, China (Nos. 52200137 and 21725102), the Plan for "National Youth Talents" and GuangDong Basic and Applied Basic Research Foundation (No. 2021A1515110427).

Supplementary materials

Supplementary material associated with this article can be found, in the online version, at doi:10.1016/j.cclet.2023.109219.

References

[1] T. Salthammer, S. Mentese, R. Marutzky, Chem. Rev. 110 (2010) 2536–2572.
[2] X. Tang, Y. Bai, A. Duong, et al., Environ. Int. 35 (2009) 1210–1224.
[3] X. Lv, J. Liu, T. Shao, et al., Catal. Today 420 (2023) 114188.
[4] J. Ye, Y. Yu, J. Fan, et al., Environ. Sci.: Nano 7 (2020) 3655–3709.
[5] R. Chen, Z. Sun, C. Hardacre, et al., Catal. Rev. 64 (2022) 1–56.
[6] S. Zhang, Y. Zhuo, C.I. Ezugwu, et al., Environ. Sci. Technol. 55 (2021) 8341–8350.
[7] Y. Zhuo, X. Guo, W. Cai, et al., Appl. Catal. B 333 (2023) 122789.
[8] L. Zhang, Q. Bao, B. Zhang, et al., JACS Au 2 (2022) 1651–1660.
[9] J. Guo, C. Lin, C. Jiang, et al., Appl. Surf. Sci. 475 (2019) 237–255.
[10] B. Qiao, A. Wang, X. Yang, et al., Nat. Chem. 3 (2011) 634–641.
[11] S. Peng, Y. Rao, Y. Huang, et al., Catal. Sci. Technol. 12 (2022) 4001–4011.
[12] H. Jin, K. Zhou, R. Zhang, et al., Nat. Commun. 14 (2023) 2494.
[13] Z. Jin, P. Li, Y. Meng, et al., Nat. Catal. 4 (2021) 615–622.
[14] M. Liu, J. Liu, Z. Li, et al., J. Catal. 370 (2019) 21–29.
[15] D. Huang, Y. Luo, S. Li, et al., Mater. Horiz. 7 (2020) 970–986.
[16] Q. Cheng, K. Mao, L. Ma, et al., ACS Energy Lett. 3 (2018) 1205–1211.
[17] Q. Cheng, S. Han, K. Mao, et al., Nano Energy 52 (2018) 485–493.
[18] X. Wang, S. Feng, W. Lu, et al., Adv. Funct. Mater. 31 (2021) 2104243.
[19] J. Zhang, X. Dong, W. Xing, et al., Chem. Eng. J. 420 (2021) 129938.
[20] Y. Zhao, H. Zhou, W. Chen, et al., J. Am. Chem. Soc. 141 (2019) 10590–10594.
[21] H. Yang, Y. Wu, G. Li, et al., J. Am. Chem. Soc. 141 (2019) 12717–12723.
[22] G. Qu, P. Jia, T. Zhang, et al., Chemosphere 288 (2022) 132594.
[23] S. Peng, X. Yang, J. Strong, et al., J. Hazard. Mater. 396 (2020) 122750.
[24] X. Yang, X. Yu, M. Lin, et al., J. Mater. Chem. A 5 (2017) 13799–13806.
[25] Q. Wang, X. Huang, Z.L. Zhao, et al., J. Am. Chem. Soc. 142 (2020) 7425–7433.
[26] Y. Chen, B. Xi, M. Huang, et al., Adv. Mater. 34 (2022) 2108621.
[27] X. Sun, J. Lin, Y. Wang, et al., Appl. Catal. B 268 (2020) 118741.
[28] Y. Li, X. Chen, C. Wang, et al., ACS Catal. 8 (2018) 11377–11385.
[29] S. Kang, M. Wang, N. Zhu, et al., Chin. Chem. Lett. 30 (2019) 1450–1454.
[30] J. Yan, J. Peng, L. Lai, et al., Environ. Sci. Technol. 52 (2018) 14302–14310.
[31] J. Wang, D. Wang, Z. Song, et al., Energy Environ. Sci. 16 (2023) 3146–3157.
[32] S. Peng, R. Li, Y. Huang, et al., Appl. Surf. Sci. 600 (2022) 154056.
[33] T. Kecskés, J. Raskó, J. Kiss, Appl. Catal. A 273 (2004) 55–62.
[34] H. Wu, Y. Song, Y. Liu, et al., J. Catal. 424 (2023) 152–161.